applied sciences

MDPI

Article

Design and Numerical Analysis of Recuperator for a Liquid Carbon Dioxide Energy Storage System

Zhao Liu [1], Min Wang [1], Yu Song [1] and Mengjuan Xu [2,*]

[1] Shaanxi Engineering Laboratory of Turbomachinery and Power Equipment, Institute of Turbomachinery, School of Energy & Power Engineering, Xi'an Jiaotong University, Xi'an 710049, China; liuzhao@mail.xjtu.edu.cn (Z.L.)

[2] School of Mechanical Engineering, Xi'an Jiaotong University, Xi'an 710049, China

* Correspondence: mengjuanxu@xjtu.edu.cn

Abstract: A liquid carbon dioxide energy storage (LCES) system has the characteristic of compact structure and easy liquefaction. As a component of heat recovery in the LCES system, the recuperator plays a crucial role in influencing the round trip efficiency (RTE) of the energy storage system, but very little attention has been paid to it even though its operation conditions are quite different from other thermal systems. In this case, the thermal and hydraulic design of the recuperator in the LCES system was completed. The flow characteristics and thermal performance of the recuperator under design conditions were analyzed, and the effects of operating at various loads on the flow characteristics and thermal performance of the recuperator were investigated. It was found that from the inlet to the outlet, the resistance coefficient of CO_2 on the cold side increased gradually while decreasing gradually on the hot side. Down the flow direction, the average temperature of CO_2 on the cold side increased sharply, while decreasing slowly in the hot side. When the systems discharged with varying loads, the pressure drop increased along both channels, but the resistance coefficient decreased gradually on both channels. The heat transfer coefficient (*HTC*) increased gradually on both sides too. The Nusselt number (*Nu*) in the first half of the cold side did not change much, while increasing gradually in the second half, but it continued to increase on the hot side.

Keywords: liquid carbon dioxide energy storage system; PCHE; numerical analysis; thermal and hydraulic design; flow and heat transfer characteristics

Citation: Liu, Z.; Wang, M.; Song, Y.; Xu, M. Design and Numerical Analysis of Recuperator for a Liquid Carbon Dioxide Energy Storage System. *Appl. Sci.* **2023**, *13*, 13151. https://doi.org/10.3390/app132413151

Academic Editors: Feng Zhang, Yong Li and Wu Jin

Received: 7 November 2023
Revised: 30 November 2023
Accepted: 9 December 2023
Published: 11 December 2023

1. Introduction

A compressed carbon dioxide energy storage system (CCES) is one of compressed gas energy storage that relies on the sCO_2 Brayton cycle. Compared with the compressed air energy storage system (CAES) [1] and LAES [2], the CCES is easier to liquefy and denser. Since Professor Morandin et al. [3] raised a system combining the trans-critical CO_2 cycle with the thermo-electrical energy storage system (TEES), many scholars dedicated themselves to the study of CCES. In 2015, Wang et al. [4] proposed a transcortical CCES with heat storage. During the charging time, the gaseous carbon dioxide was pressurized by a set of compressors, and the compression heat was retained in a heat accumulator, then cooled by a throttle valve, and finally condensed into liquid through a condenser. During the discharging time, the pump was utilized to pressurize the liquid CO_2. After the high-pressure CO_2 absorbed heat in the recuperator, it became gas and then expanded in the turbine to do work. Finally, the exhaust gas was further condensed into liquid, and stored in a tank.

Subsequently, Zhang et al. [5] proposed a CCES derived from the trans-critical CO_2 Brayton cycle. The thermodynamic model was developed and the thermodynamic performance was studied. The RTE of the system was lower compared to the adiabatic CAES (ACAES), but the storage density was 2.8 times that of ACAES. Liu et al. [6] contrastively analyzed the performance of ACAES, CAES, and CCES with a similar system arrangement. It was concluded that the RTE was lower than the RTE of the corresponding CAES when CO_2 was stored in gas, while it was higher than LAES after the carbon dioxide was stored as liquid, and the storage temperature was more easily reached. Alami et al. [7] conducted a charge and discharge experiment of CCES with three 7 L cylinders. The maximum storage pressure was 0.3 MPa. The overall efficiency of the system was 46.2%. It was concluded that CCES had obvious advantages regarding efficiency and footprint compared with similar CAES systems.

Some scholars have combined CCES with other cycling systems for better thermal performance. A transcortical CCES combined with a cooling heating and power (CCHP) system that utilized waste heat was proposed by Zhang et al. [8]. It was noted that system power efficiency and system energy efficiency were 0.48 and 1.19, respectively. The energy density was 11.51 kWh/m^3.

Despite the fact that the CCES is generally acknowledged as a promising energy storage system, most works focus on the thermodynamic analysis of system integration, and further design of components for the system is not enough. The key components of CCES include heat storage devices, turbomachinery, and efficient heat exchangers. Among them, PCHE, a high-effectiveness heat exchanger, was first proposed in the 1980s and manufactured by Haynes in 1985 [9]. Subsequently, PCHE has been widely studied in the sCO_2 power cycle for its compact structure and efficiency, since Dostal et al. [10] published the study of the sCO_2 cycle, and the PCHE was adopted to transfer heat.

It was found that the channel structures greatly impact the performance of the PCHE, then a lot of work on geometric structure optimization has been carried out. The common channel shapes include straight, U, Z, and S shapes. Meshram. et al. [11] compared the influence of a straight shape and a zigzag-shaped channel, and it can be observed that the channel diameter and Reynolds number had a significant impact on the pressure loss of working fluid. For the zigzag channel, increasing the bending angle and decreasing the linear pitch could benefit the performance of PCHE. The thermal performance of the Z-shaped channel was obviously superior to that of the straight channel while obtaining a larger drop loss. A sinusoidal shape channel PCHE was studied by Wen et al. [12]. In comparison with the straight-through channel, the sinusoidal shape was more beneficial for the heat transfer performance of the exchanger. Moreover, the heat transfer performance increased with the growth of amplitude and the decrease in wavelength. The flow distribution of a PCHE was studied in the literature [13]. The impacts of flow uniformity were suited by numerical simulations. The inlet header designed in the shape of a taper was optimized. It was concluded that the appropriate cone angle can make the flow distribution more uniform, resulting in improving the heat transfer property of PCHE by 17.3–19.7%.

When pressure and temperature differences between PCHE channels are too large, it is easy to cause channel dispatching. The stress deviation of the main PCHE channels in the power generation system was studied by Simanjuntak et al. [14] when the pressure difference between the PCHE channels was 19.5 Mpa and the temperature difference was 25 °C. The result showed that the stress intensity grew with the increase in misalignment. It is less safe than the condition without misalignment.

Furthermore, some experimental research has been performed. The pressure resistance, leakage, corrosion conditions, flow characteristics, and thermal performance of PCHE with CO_2 as a working fluid were tested. Xin et al. [15] simulated the impacts of channel width, pressure of spray, corrosion temperature, and corrosion time, by combining numerical simulation and experiment. Chu et al. [16] fabricated straight-channel PCHE heat exchangers in two ways, diffusion bonding technology and photochemical etching technology. Under the same experimental conditions, the heat transfer and hydraulic properties using CO_2 and water as working mediums, respectively, were compared. The results showed that sCO_2 had better performance. The PCHE using CO_2 as a working fluid under different pressures was also studied by experiments. The finding revealed that the PCHE had better comprehensive performance when the pressure of CO_2 was higher.

The PCHE was adopted as a precooler in a 100 kW class CO_2 Brayton cycle by Cheng et al. [17]. Zigzag fins are adopted on both sides of the PCHE, arranged in a single row. Under various Reynolds numbers and temperatures, the heat transfer coefficient (*HTC*) and pressure drop of the PCHE were tested. Kwon et al. [18] studied the PCHE *HTC* of a small channel PCHE through experiments. A two-layer-channel PCHE with a channel hydraulic diameter of 1.83 mm was machined as a testing sample. The *HTC* of boiling heat transfer, single-phase heat transfer, and condensation heat transfer were studied and compared under different temperatures.

Given the above, there has been extensive research on the influence of channel structure and processing technology on the effectiveness of PCHE. However, in the process of numerical simulation or experiment, a unilateral channel with a constant value of wall temperature or heat flow was generally considered. Normally there was water or other working fluid on one side, and CO_2 on the other side. Only a few researchers carried out research with carbon dioxide on both sides and the temperature of the CO_2 did not vary much according to their research. However, for the LCES [19] investigated in this study, the state of CO_2 flowing in the recuperator on the cold side varied from liquid to supercritical, and the physical properties of the CO_2 changed sharply. Therefore, it is very important to establish an accurate model and study the heat transfer and fluid performance of the PCHE used as a recuperator, which is helpful for the performance evaluation of the LCES.

For this study, the thermodynamic model of a printed circuit recuperator used in the LCES was studied, and the thermal design of the recuperator was completed. The flow characteristics and thermal performance of the recuperator under design conditions were analyzed, and the impacts of different loads on the thermal performance of the recuperator were implemented.

2. Boundary Conditions and Geometric Structure Design

The PCHE channels are typically fabricated by chemically etching on metal plates and then bonded together through diffusion bonding. The most common channel shapes include semicircular, triangular, trapezoidal, etc., and their cross-sectional diameter is in the range of 0.5 to 2 mm. In the present paper, the classical structure of a semicircular straight channel is adopted, as illustrated in Figure 1.

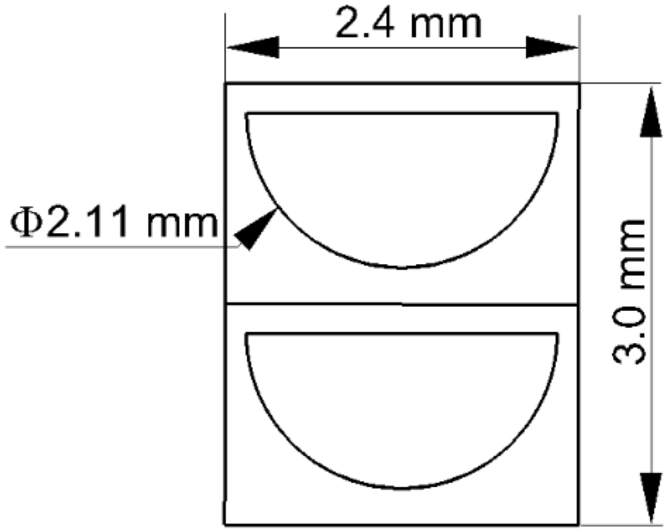

Figure 1. Schematic of PCHE channel structure.

In a thermal and hydraulic design, the entire PCHE was discretized into several small segments based on equal thermal load units. By employing the logarithmic mean temperature difference (LMTD), the geometric parameters of each segment were calculated, and the geometric size of the recuperator could be derived.

In this paper, the PCHE was divided into 80 segments for calculation. The heat transfers in each segment "i" can be calculated using the following formula:

$$Q_i = U_i A_i \Delta T_{lmtd,i} \tag{1}$$

where Q_i is the heat transfer capacity in segment "i", U_i is the overall HTC, A_i is the surface area, and $\Delta T_{lmtd,i}$ is the LMTD.

The LMTD is expressed as:

$$\Delta T_{lmtd} = \frac{(\Delta T_L - \Delta T_M)}{\ln(\Delta T_L / \Delta T_M)} \tag{2}$$

where ΔT_L is the larger temperature difference and ΔT_M is the smaller difference in temperature.

The HTC, U, is calculated as follows:

$$\frac{1}{U} = \frac{1}{h_{hx,cool}} + \frac{1}{h_{hx,hot}} + \frac{\delta_p}{\lambda_p} + R_w \tag{3}$$

where $h_{hx,cool}$ is the convective HTC of CO_2 on the cold channel, $h_{hx,hot}$ is the convective HTC on the hot side, δ_p is the thickness of the wall, λ_p is the thermal conductivity of solid material, and R_w is the fouling thermal resistance.

The convective HTC is given as:

$$h_{hx} = \frac{\lambda_f \cdot Nu}{D_h} \tag{4}$$

The hydraulic diameter for a semicircular structure can be defined as follows:

$$D_h = \frac{4S_c}{C_c} \tag{5}$$

where S_c is the area of cross-section and C_c is the circumference.

The Nu in PCHE is obtained utilizing the Gnielinski correlation formula [20], which is expressed as follows:

$$\begin{cases} Nu = 4.089(Re < 2300) \\ Nu = 4.089 + \frac{Nu_{5000} - 4.089}{5000 - 2300}(2300 \le Re < 5000) \\ Nu = \frac{(f_d/8)(Re - 1000)Pr}{1 + 12.7\left(Pr^{2/3} - 1\right)\sqrt{f_d/8}}(Re \ge 5000) \end{cases} \tag{6}$$

where

$$f_d = (1/(1.8\log 10(\mathrm{Re}_1) - 1.5))^2 \tag{7}$$

where Pr is the Prandtl number.

After obtaining the surface area of the heat exchanger, the length can be derived as follows:

$$L = \frac{A}{(0.5\pi D + D)\ N} \tag{8}$$

where D is the diameter of the semicircular channel and N is the number of channels.

On the premise of the foregoing calculations, the pressure drop can be deduced as follows:

$$\Delta p = \frac{f \cdot L \cdot G^2}{2D_h \cdot \rho} \tag{9}$$

where f is the friction factor and G is the mass flow rate.

The inlet and outlet parameters for the thermal design of the PCHE are shown in Table 1.

Table 1. Inlet and outlet thermodynamic parameters of the PCHE.

Parameters	Hot-Side Inlet	Cold-Side Inlet
Temperature/K	674.3	298.2
Pressure/MPa	6.5	25
Mass Flow Rate/kg·s^{-1}	62.19	62.19

The geometric results of the PCHE are illustrated in Table 2.

Table 2. Values and calculated results of channel geometric structure.

Parameters	Value	Parameters	Value
Channel Diameter/mm	2.11	Number of Cold Channels	7.6×10^4
Horizontal Spacing/mm	2.4	Length/m	1.72
Metal Plate Thickness/mm	1.5	Cold-Side Pressure Drop/kPa	42.8
Number of Hot Channels	7.6×10^4	Hot-Side Pressure Drop/kPa	58.2

3. Numerical Calculation Method and Validation of Numerical Method

The ANSYS CFX was applied for the numerical calculations in this study. Kader's wall function law was employed to handle the thermal boundary layer on the walls. The dimensionless temperature is given as:

$$T^{+} = \frac{\rho c_p u^* \left(T_W - T_f\right)}{q_W} \tag{10}$$

where T_W and T_f are the temperatures of the wall and near-wall, respectively. q_W is the heat flux density of the wall/W·m^{-2}.

The dimensionless temperature distribution [21] can be modeled as:

$$T^{+} = \mathrm{Pr} y^* e^{(-\Gamma)} + [2.12 \ln(y^*) + \beta] e^{(-1/\Gamma)} \tag{11}$$

where

$$\beta = \left(3.85 \mathrm{Pr}^{1/3} - 1.3\right)^2 + 2.12 \ln(\mathrm{Pr}) \tag{12}$$

$$\Gamma = \frac{0.01 (\mathrm{Pr} y^*)^4}{1 + 5 \mathrm{Pr}^3 y^*} \tag{13}$$

The Pr is defined as:

$$\mathrm{Pr} = \frac{\mu c_p}{\lambda} \tag{14}$$

where λ is the thermal conductivity of the working medium.

Based on Equations (11)–(14), the wall heat flux model can be expressed as:

$$q_w = \frac{\rho c_p u^*}{T^+} \left(T_W - T_f\right) \tag{15}$$

3.1. Verification of Turbulence Model for Geometric Structure

Turbulence models are established on a series of assumptions; thus, different turbulence models are required for different physical models. The turbulence model has a great impact on the calculation results. Therefore, the numerical simulation for the recuperator discussed in this paper is needed to verify the results obtained using various turbulence models with experimental results. This verification of turbulence mode is essential to ensure the dependability of subsequent simulation results.

The turbulence model was verified by using experimental results of heat transfer characters for PCHE conducted by Nikitin et al. [22] and Ngo et al. [23] from the Tokyo Institute of Technology, Japan. Figure 2a presents the experimental setup, the geometric structure, and the arrangement of the heat exchanger test section. The PCHE test section consisted of 12 layers with a total of 144 channels for CO_2 on the hot side and 6 layers with a total of 66 channels on the cold side. The core dimensions were 71 × 76 × 896 mm^3. The channel arrangement is exhibited in Figure 2b, and the specific structure and dimensions of the channels on both sides are shown in Figure 2c. A Z-shaped flow path was utilized in the experiments, and the specific parameters of the structure are illustrated in Table 3. During the experiments, the pressure and temperature ranges for CO_2 on the hot side were 2.2–3.2 MPa and 280–300 °C, respectively, and on the cold side, the ranges were 6.5–10.5 MPa and 90–108 °C, respectively. The mass flow rates on both sides were the same, varying from 40 to 80 kg·h^{-1}. Finally, Nikitin et al. [22] provided experimental data in the open literature under the conditions of 108 °C on the cold side and 280 °C on the hot side.

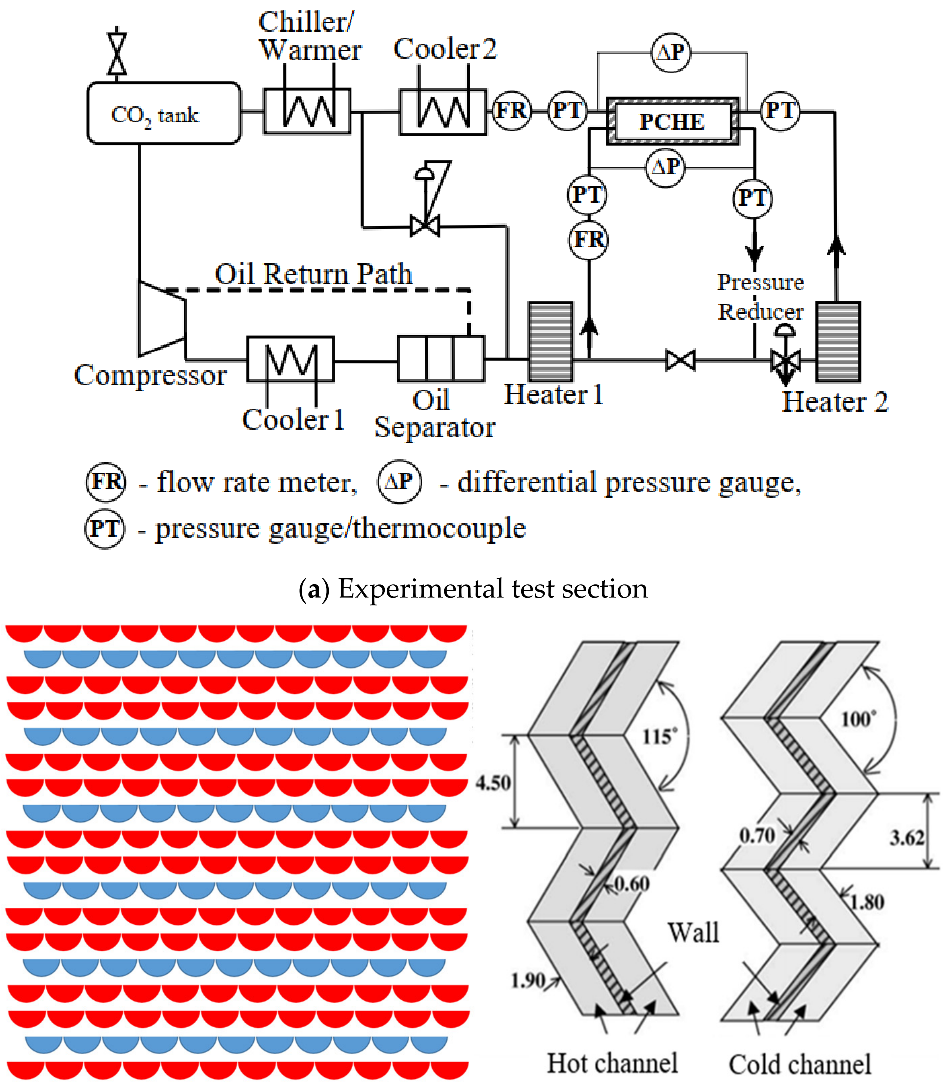

(**a**) Experimental test section

(**b**) Flow channel configuration (**c**) Flow channel dimensions

Figure 2. Experimental test facility of PCHE [22,23].

Table 3. PCHE geometric data in the experiments conducted by Nikitin et al. [22].

	Channels	Diameter/mm	Angle/°	Segment Length/mm	Effective Length/mm	Core Length/mm
Hot side	144	1.9	32.5	4.5	1000	896
Cold side	66	1.8	40	3.62	1100	896

It would require a large amount of computation if the same structure was adopted in numerical simulation as tested by Nikitin et al. Referring to the research experience provided by Kim et al. [24,25], the experimental model can be simplified to one cold and one hot model with angles of 32.5° or 40.0°, respectively. The schematic diagram illustrating the corresponding structures compared with the experiments is shown in Figure 3. Therefore, to further reduce the number of grids and consequently decrease the computational demand, the length of the flow path in the heat exchanger for this paper was also shortened from the original 896 mm to 54 mm. The geometric parameters of the models used for the final validation of the turbulence model are presented in Table 4.

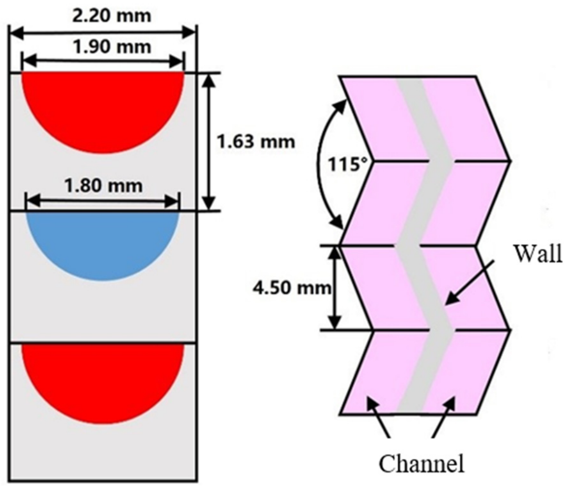

Figure 3. Geometry of the PCHE unit used in the validation calculation.

Table 4. Geometry of the PCHE used for turbulence model validation.

	Channels	Diameter/mm	Angle/°	Segment Length/mm	Length/mm
Hot Side	2	1.9	32.5	4.5	54
Cold Side	1	1.8	32.5	4.5	54

3.2. Computational Meshes and Boundary Conditions

The tetrahedral unstructured grid utilized in the validation model calculation was generated using ANSYS ICEM. To improve the grid quality, prism grids were employed near all wall surfaces. For low Reynolds number turbulence models based on the ω equation, it is required that the value of y^+ near the wall be less than 1. Therefore, the thickness from the first mesh layer of the cold-side fluid to the wall surface was set to 0.0001 mm, and 32 layers of prism grids were arranged in the vertical wall direction with a grid expansion ratio of 1.2. Similarly, for the hot side fluid, the distance from the initial mesh to the wall surface was defined as 0.0002 mm, and 28 layers of prism grids were placed in the vertical wall direction with a grid expansion ratio of 1.2. The thickness between the first mesh at the solid–fluid interface and the boundary was the same as that on the corresponding fluid side, and 8 layers of prism grids were arranged in the vertical boundary direction. The count of grid nodes was around 3.081 million, and the total number of elements was approximately 6.58 million. For high Reynolds number turbulence models based on the ε equation, the first layer grid adjacent to the wall needed to be placed in the area of intense turbulence. In this case, a two-layer prism grid was used, and the distance from the initial layer grid to the wall surface was defined as 0.1 mm and y^+ was controlled between 12 and 80. On the solid–fluid interface, the initial layer grid was set at the same distance from the boundary as on the corresponding fluid side, and 1 layer of prism grid was arranged vertically along the boundary direction. The total number of grid nodes was approximately 398,000 and the count of elements was around 1.216 million.

ANSYS CFX was performed in the calculations process, and boundary conditions were consistent with those of Nikitin et al. [22]. The inlet pressure was set to 3.2 MPa for the cold side and 10.5 MPa for the hot side. The inlet temperature on the hot side was 280 °C. Figure 4 displays the temperature distribution, with the computational range limited to 0 to 0.054 m. Therefore, according to Figure 4, the cold-side inlet temperature of CO_2 was set to 221.8 °C, which corresponds to the temperature at the location of 0.054 m. The inlet turbulence intensity was set to 5% for both channels. The mass flow rate boundary conditions were specified at the outlets of both channels, with the total flow rate being the same. A total of 13 operating conditions were calculated over the mass flow rate scope of 30–390 kg·h^{-1}. The fluid–solid interface was defined as a coupled heat transfer boundary. Periodic boundaries were set to the left-right and top-bottom surfaces. The total energy model was adopted for the fluid domain in the calculations. The properties of CO_2 were obtained from the RGP property parameter table derived from NIST. The solid domain was modeled using a thermal energy model that neglects density variations during the solution process. "Steel" was set as the material from the material library, and λ is 16.2 W·m^{-2}·K^{-1}.

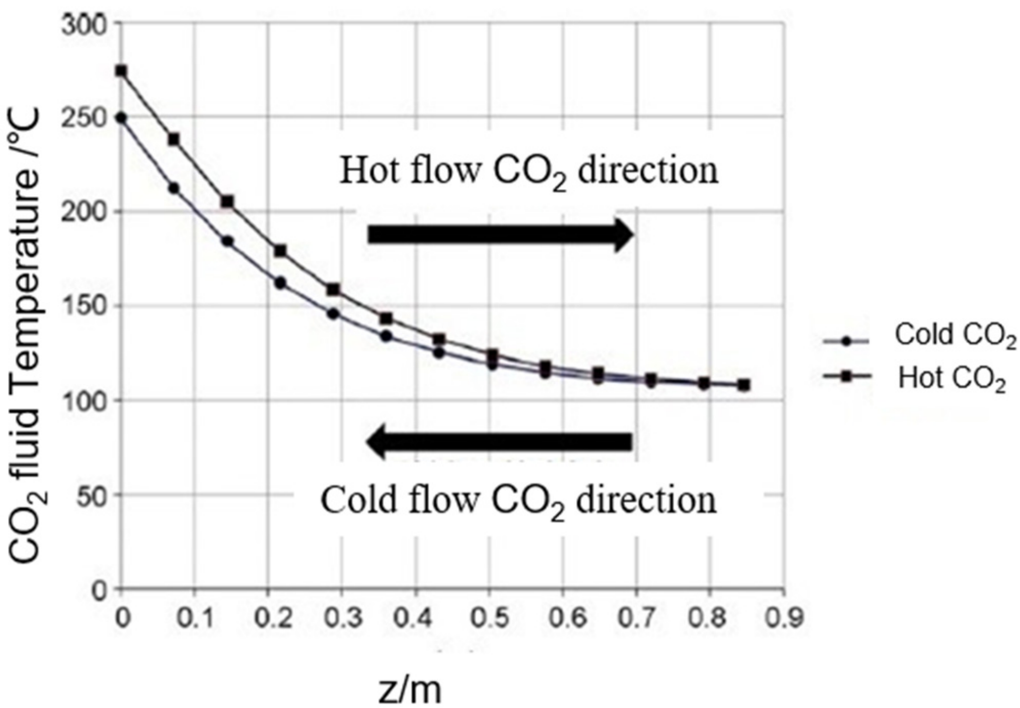

Figure 4. Temperature variation of carbon dioxide along the length on the cold and hot sides calculated by Kim et al. [26].

3.3. Comparison of Computational Results with Experimental Results

The SST k-ω model, standard k-ε model, and the RNG k-ε model had been applied in previous studies of supercritical CO_2 PCHE. Therefore, these four turbulence models need to be validated in this study. The results obtained from these four turbulence models contrast with the experimental correlations provided by Nikitin et al. [22], Ngo et al. [23], Ishizuka et al. [27], and Hesselgreaves et al. [28], as well as the correlations fitted based on numerical results by Kim et al. [25]. The specific empirical formulas and their applicable ranges are shown in Table 5.

The results were processed using the same method as Kim et al. [25], obtaining the friction coefficients and *Nu* under different operating conditions.

Figures 5 and 6 provide a comparative analysis of the calculated friction factors and *Nu* with the experimental correlations provided by Nikitin et al. [22], Ngo et al. [23], Ishizuka et al. [27], and Hesselgreaves et al. [28], as well as the correlation equations adapted by Kim et al. [25]. The friction factors and *Nu* were calculated for Reynolds numbers (*Re*) on the cold side ranging from 4200 to 55,000 and from 1800 to 24,000 on the hot side. It should be noted that Hesselgreaves' experimental correlation equations consist of two segments for the applicable Reynolds number range, which are represented by two separate lines. On the other hand, the experimental correlations by Nikitin et al. and Ngo et al. and the numerical correlation equation by Kim et al. [25] were all single range. The upper and lower limits of the correlation equations were represented by solid and dashed lines with the same color.

Table 5. Empirical formulas for local convective HTC/Nu and friction factors provided by different researchers.

Researcher	Local h or Nu	Friction Factor f	Applicability
Nikitin et al. [22]	$h_h = 2.52\mathrm{Re}^{0.681}$	$f_h = (-1.402 \times 10^{-6} \pm 0.087 \times 10^{-6})\mathrm{Re} + (0.04495 \pm 0.00038)$	$2800 \leq \mathrm{Re} \leq 5800$
	$h_c = 5.49\mathrm{Re}^{0.625}$	$f_c = (-1.545 \times 10^{-6} \pm 0.099 \times 10^{-6})\mathrm{Re} + (0.09318 \pm 0.00090)$	$6200 \leq \mathrm{Re} \leq 12{,}100$
Ngo et al. [23] Angle 52°	$\mathrm{Nu} = (0.1696 \pm 0.0144)\mathrm{Re}^{0.629 \pm 0.009} \times \mathrm{Pr}^{0.317 \pm 0.014}$	$f_h = (0.3390 \pm 0.0285)\mathrm{Re}^{-0.158 \pm 0.009}$ $f_c = (0.3749 \pm 0.1293)\mathrm{Re}^{-0.154 \pm 0.036}$	$3500 \leq \mathrm{Re} \leq 22{,}000$ $0.75 \leq \mathrm{Pr} \leq 2.2$
Ishizuka et al. [27] Angle 32.5°	$h_h = 0.2104\mathrm{Re} + 44.160$	$f_h = -2.0 \times 10^{-6}\mathrm{Re} + 0.0467$	$2400 \leq \mathrm{Re} \leq 6000$
	$h_c = 0.1106\mathrm{Re} + 15.943$	$f_c = -2.0 \times 10^{-6}\mathrm{Re} + 0.1023$	$5000 \leq \mathrm{Re} \leq 13{,}000$
Hesselgreaves et al. [28]	$\mathrm{Nu} = 0.4\mathrm{Re}^{0.60}\mathrm{Pr}^{1/3}\cdot(2D/l)^{0.75}$ $\mathrm{Nu} = 0.4\mathrm{Re}^{0.64}\mathrm{Pr}^{1/3}\cdot(2D/l)^{0.75}$ D channel width, l channel pitch	$f = 2.0\mathrm{Re}^{-0.40}\cdot(2D/l)^{0.75}$ $f = 4.8\mathrm{Re}^{-0.36}\cdot(2D/l)^{1.50}$	$600 < \mathrm{Re} < 3000$ $10^4 < \mathrm{Re} < 10^5$
Kim et al. [25] Angle 32.5°	$\mathrm{Nu} = (0.0292 \pm 0.0015)\mathrm{Re}^{0.8138 \pm 0.0050}$	$f = (0.2515 \pm 0.0097)\mathrm{Re}^{-0.2031 \pm 0.0041}$	$2000 \leq \mathrm{Re} \leq 58{,}000$ $0.7 \leq \mathrm{Pr} \leq 1.0$

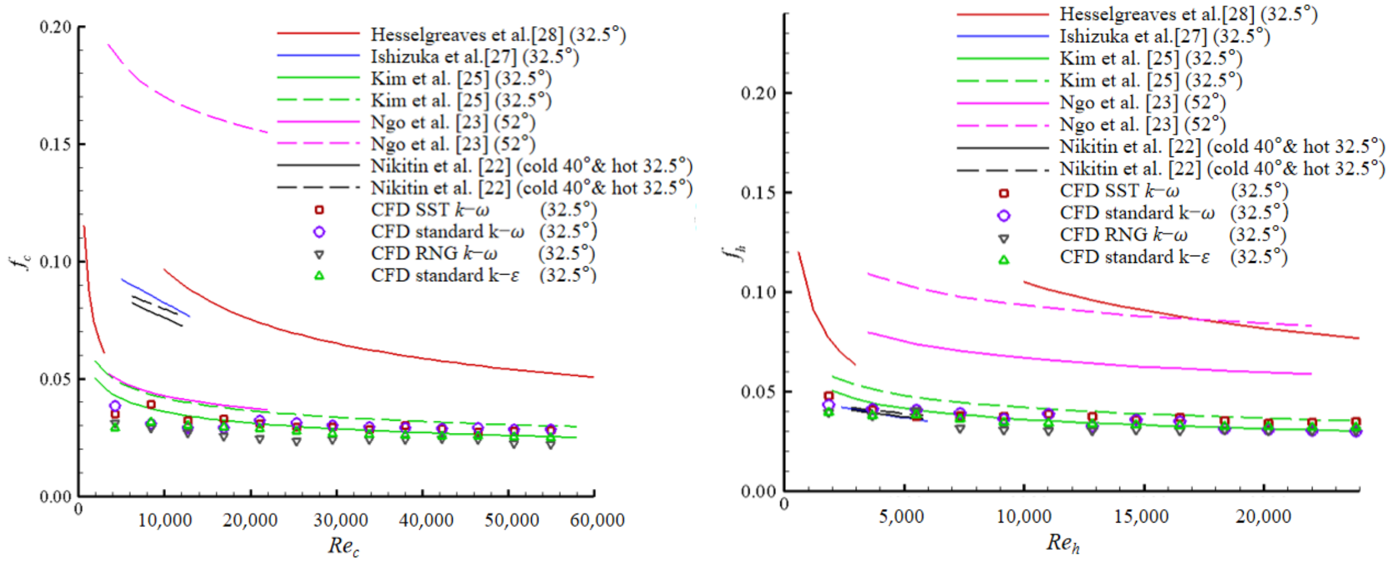

(**a**) Cold side (**b**) Hot side

Figure 5. Comparison of numerical calculation results of the friction factors on both channels with the experimental correlation equation.

Figure 5 reveals that four turbulence models can accurately compute the friction factors of the PCHE. The numerical calculation results for the cold side were in general accordance with the experimental findings of Ngo et al. The numerical results for the hot side were in line with the experimental findings by Ishizuka et al. and Nikitin et al. Moreover, the numerical calculation results for both channels exhibited excellent conformity with those of Kim et al. In terms of simulation accuracy, the friction coefficients calculated employing the ε equation-based high Reynolds number model were slightly lower, which is similar to the findings obtained by Abel et al. [25]. Results calculated with the standard k-ω and SST k-ω models displayed better agreement with experimental values. Compared to the standard k-ω model, the results obtained employing the SST k-ω model were more similar to the experimental data t. Additionally, Figure 6 shows that all four turbulence models can accurately compute the characters of the PCHE. The computational results for the *Nu* on both channels reveal excellent consistency with the experimental findings as well as the numerical results by Kim et al.

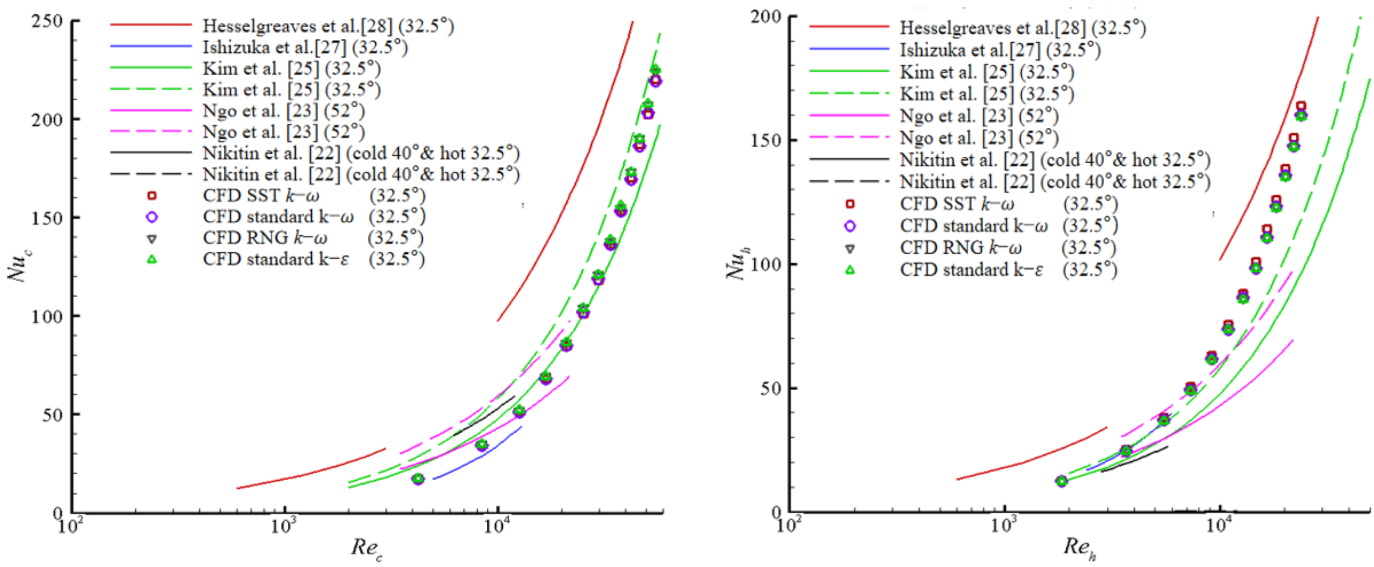

(**a**) Cold side (**b**) Hot side

Figure 6. Comparison of CFD results with experimental correlation equation results for Nusselt numbers.

By comparing the experimental and numerical correlations of the friction factors and *Nu* for varying Reynolds numbers, it is found that the results obtained utilizing the four turbulence models are reliable. Furthermore, considering that the friction coefficients calculated employing the SST k-ω model closely match the experimental data, the subsequent calculations will be conducted employing the SST k-ω model.

4. Numerical Model Verification of the PCHE and Mesh Independence

For this research, the validated numerical calculation method was applied to perform a numerical analysis of the effectiveness of the PCHE.

4.1. Simplified Numerical Model of the PCHE

The configuration of the PCHE designed in Section 2 is illustrated in Figure 7. The channels on the hot and cold sides are colored red and blue, respectively. The channels are arranged in a layered and spaced manner, with a total of 76,100 on each side. Each channel is 2.11 mm in diameter, 2.4 mm pitched horizontally, 1.5 mm pitched vertically, and 1726.5 mm in length. A minimum heat transfer unit was extracted from the heat exchanger for calculation to reduce the computational amount, including a cold fluid passage, and a hot fluid passage along their corresponding solid parts. To avoid the influence of uniform boundary conditions and the backflow at the outlet on the calculation, an extension section of 100 mm was added to both the inlet and outlet of the channels.

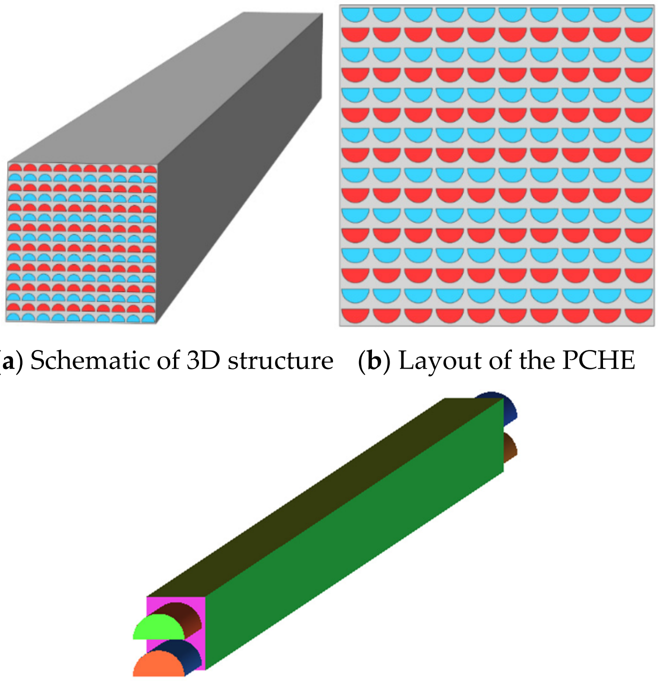

(**a**) Schematic of 3D structure (**b**) Layout of the PCHE

(**c**) Structural unit for calculation

Figure 7. The structure of the PCHE.

4.2. Mesh Independence

The study of grid independence is implemented to guarantee the reliability of numerical simulations. Thus, the numerical solutions should be studied within a relatively wide range of grid resolutions to make sure that the obtained results are not affected by the grid node. In this section, three sets of grids with different density distributions were used to explore the impacts of grid density on the simulation of the PCHE.

The calculation meshes are exhibited in Figure 8, where the orange region indicates the cold fluid field, the green zone indicates the hot fluid field, and the purple zone indicates the solid field. An O-grid was applied near the walls to improve grid quality. Since the SST k-ω turbulence model needs the value y^+ near the wall to be inferior to 2, the distance from the initial row of fluid domain cells to the wall was set to 0.0003 mm for all three sets of grids. It ensured that $y^+ \leq 1$. Additionally, all three sets of grids had more than 15 grid nodes arranged in the vertical wall direction within the boundary layer. The number of grid nodes for the three sets of grids is 3.341 million, 5.367 million, and 19.191 million, respectively. The grids are densified in all three directions at the same scale.

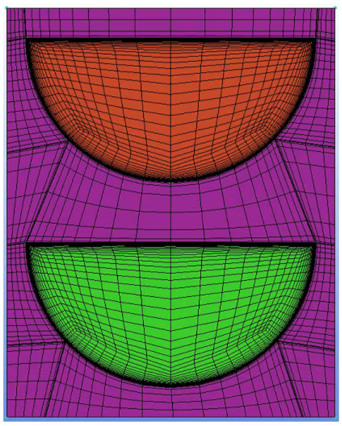

Figure 8. Grids used for calculations.

The calculations were performed by ANSYS CFX with the SST k-ω model, and the overall solution accuracy was second order. The boundary conditions for assessing mesh independence were set according to the design operating conditions. The inlet conditions were specified with mass flow rates and the outlet boundary condition was given average static pressures. The temperature of inlets was set to 298.2 K and 674.3 K, respectively. The outlet average static pressures were specified as 25 MPa for the cold side and 6.5 MPa for the hot side. The fluid–solid interface was defined as a coupled heat transfer boundary. The four sides of the model were set as periodic boundaries, and the rest of the solid walls were regarded as adiabatic walls. The fluid domain adopted the total energy model, and the thermophysical properties of carbon dioxide were obtained from two 2000 × 3000 tables derived from NIST. The pressure range for the thermophysical properties table of the cold side CO_2 is 23–27 MPa, and for the hot side, it is 4.5–8.5 MPa. The temperature range is 225–850 K. The solid domain utilized a thermal energy model that neglected density variations during the solution process, and "Steel" was selected from the material library, whose thermal conductivity is 16.2 $W{\cdot}m^{-2}{\cdot}K^{-1}$.

Three sets of grids with 3.341 million, 5.367 million, and 19.191 million grid nodes were used to simulate the flow and thermal characteristics of PCHE. The formulas for processing the calculation results are shown in Equations (13)–(15).

The results of the simulations are illustrated in Figures 9–11. The blue arrow represents the flow direction of the cold CO_2, while the red arrow indicates the flow direction of the hot CO_2.

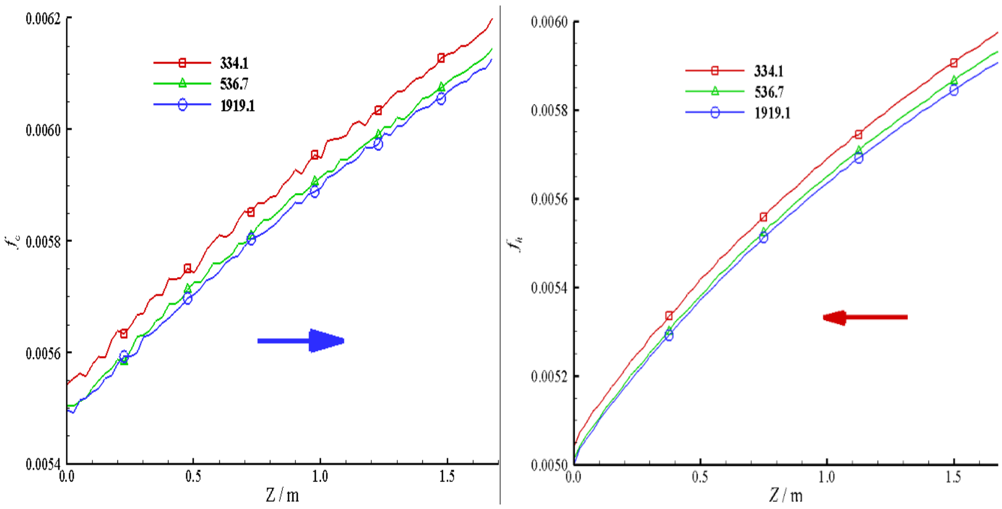

(**a**) Cold side (**b**) Hot side

Figure 9. Friction factor distributions of CO_2 along the PCHE both on the cold side and hot side for different grid numbers.

Figure 9 presents the friction factors distribution of CO_2 along the PCHE both on the cold side and hot side for different grid numbers. It can be observed that the distribution of friction factors was uniform. As the number of grids varies from 3.341 million to 19.191 million, the distribution of friction factors decreased along the PCHE, and the values of the friction factors at each node were closed. Furthermore, the results obtained using 5.367 million grids were very close to those obtained using 19.191 million grids, while the value deviation was slightly larger when using 3.341 million grids.

Figure 10 shows the temperature profiles of CO_2 simulated by different grid numbers. It is evident that the temperatures simulated by the three grids are exactly the same.

Figure 11 illustrates *Nu* distributions of CO_2 along the PCHE both on the cold side and hot side for different grid numbers. It can be found that the distribution of *Nu* was uniform, and its value slightly decreased with the increase of grid notes. On the cold side, the *Nu* of CO_2 was closed for using three different sets of grids. When the grid notes were

3.341 million, the Nu of the hot CO_2 was slightly larger than that simulated by the other two sets of grids. But the Nu were very close while simulated by the grid numbers of 5.367 million and 19.191 million.

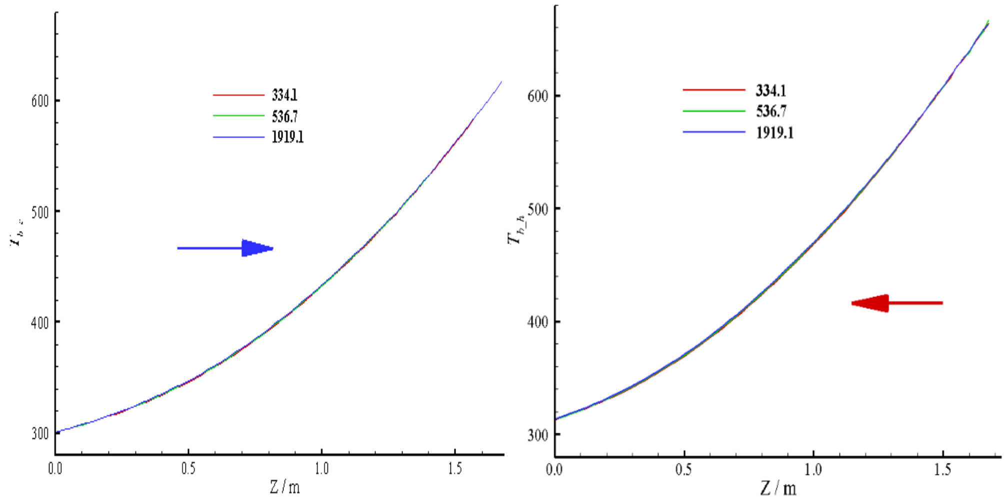

(**a**) Cold side (**b**) Hot side

Figure 10. Temperature distributions of CO_2 along the PCHE both on the cold side and hot side for different grid numbers.

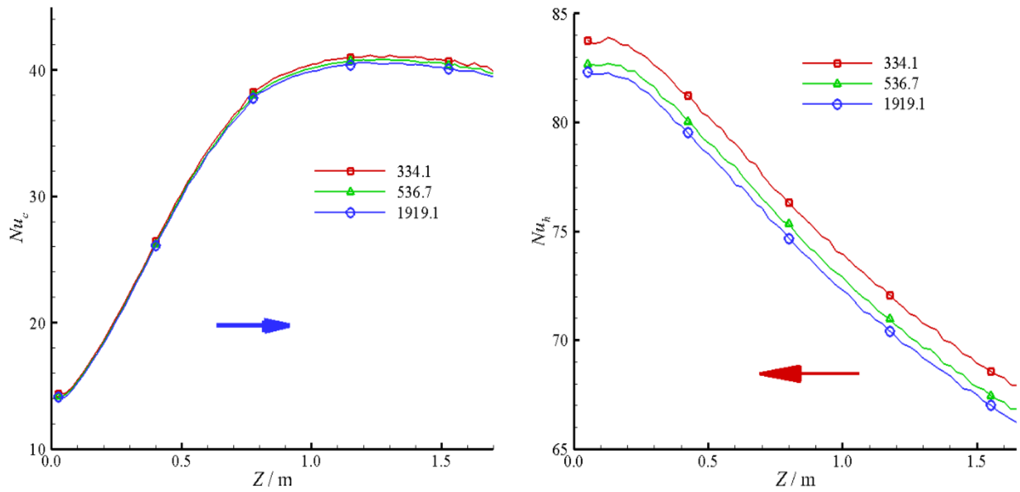

(**a**) Cold side (**b**) Hot side

Figure 11. Nusselt number distributions of CO_2 along the PCHE both on the cold side and hot side for different grid numbers.

It can be concluded that raising the number of grids beyond 5.367 million has a negligible influence on the simulated result. Therefore, it is advisable to employ a grid with a node of 5.367 million or higher for numerical computations in investigating the performance of the PCHE, for both computational accuracy and efficiency can be taken into account. In the subsequent numerical calculations, a grid with a node number of 5.367 million was employed.

4.3. Computational Grid Configuration

For the flow characteristic and thermal performance analysis of the PCHE, the simulation model and boundary parameters were set the same as discussed in the previous section. A minimum heat exchanger unit was used. The grid used for calculations was a hexahedral structured grid with a node number of 5.367 million, generated using ANSYS ICEM. An O-grid structure was employed near the walls to improve grid quality. The thickness from the first layer of fluid domain grid cells to the wall was set to 0.0003 mm to ensure value $y+ < 1$. Additionally, 23 layers of grid cells were arranged in the vertical wall direction, and the grid expansion ratio was set to 1.2.

5. Results

5.1. Flow Characteristics and Thermal Performance

Figure 12 illustrates the distribution of fluid velocities on both channels at different cross-sections along the PCHE under design conditions. The PCHE was divided into five equal parts according to length to form 6 cross-sections from the inlet to the outlet. It demonstrates a gradual increase in fluid velocity along the cold side, contrasting with a decrease on the hot side. Specifically, the average velocity at the inlet is 0.45 $m{\cdot}s^{-1}$, then rose to 1.67 $m{\cdot}s^{-1}$ at the outlet. But on the hot side, it decreases from 8.27 $m{\cdot}s^{-1}$ to 2.35 $m{\cdot}s^{-1}$, from the inlet to the outlet. This is because CO_2 exhibits relatively small pressure variations but significant temperature changes on both sides. As the temperature rises, the density of CO_2 decreases, resulting in an increasing fluid velocity.

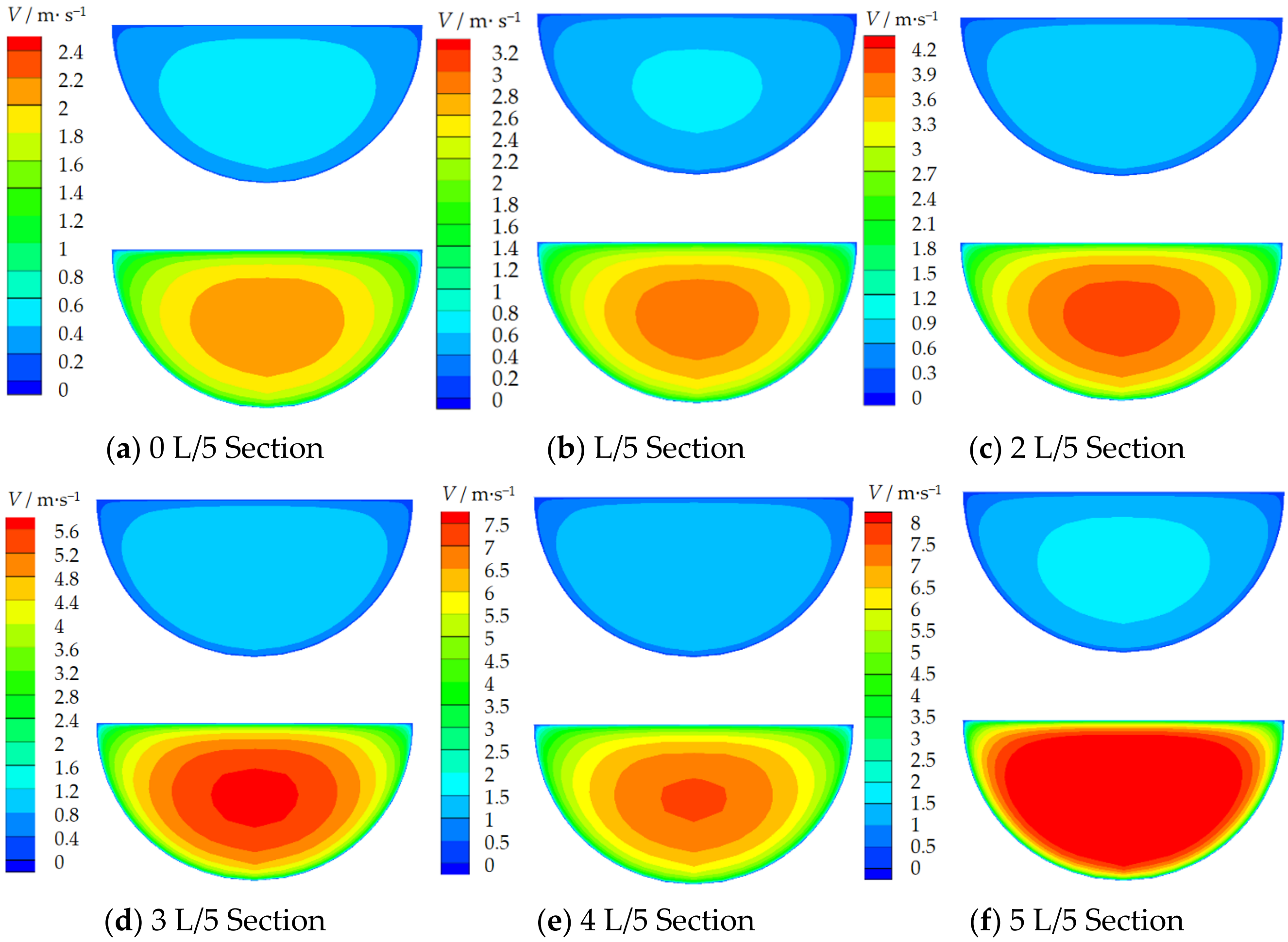

Figure 12. Distribution of CO_2 velocities along the PCHE both on the cold and hot sides at different cross-sections.

Figure 13 presents the fluid and solid domain temperature profiles at different cross-sections of the PCHE under design conditions. The six cross-sections were formed by equally dividing the PCHE into five parts according to the cold side. The upper channel represents the cold side, and the lower channel represents the hot channel. Figure 13 reveals that the temperature of CO_2 on the hot side gradually decreases while increasing on the cold side from the center to the wall. There is a significant thermal resistance between the solid and fluid domains, and the temperature gradient inside the fluid domains is larger than that of the solid material. This is due to the higher thermal conductivity of the solid material compared to the fluid, but a lower convective *HTC* between the fluid and the solid. Along the direction of CO_2, the temperature of CO_2 on the cold side gradually increases, while gradually decreasing on the hot side.

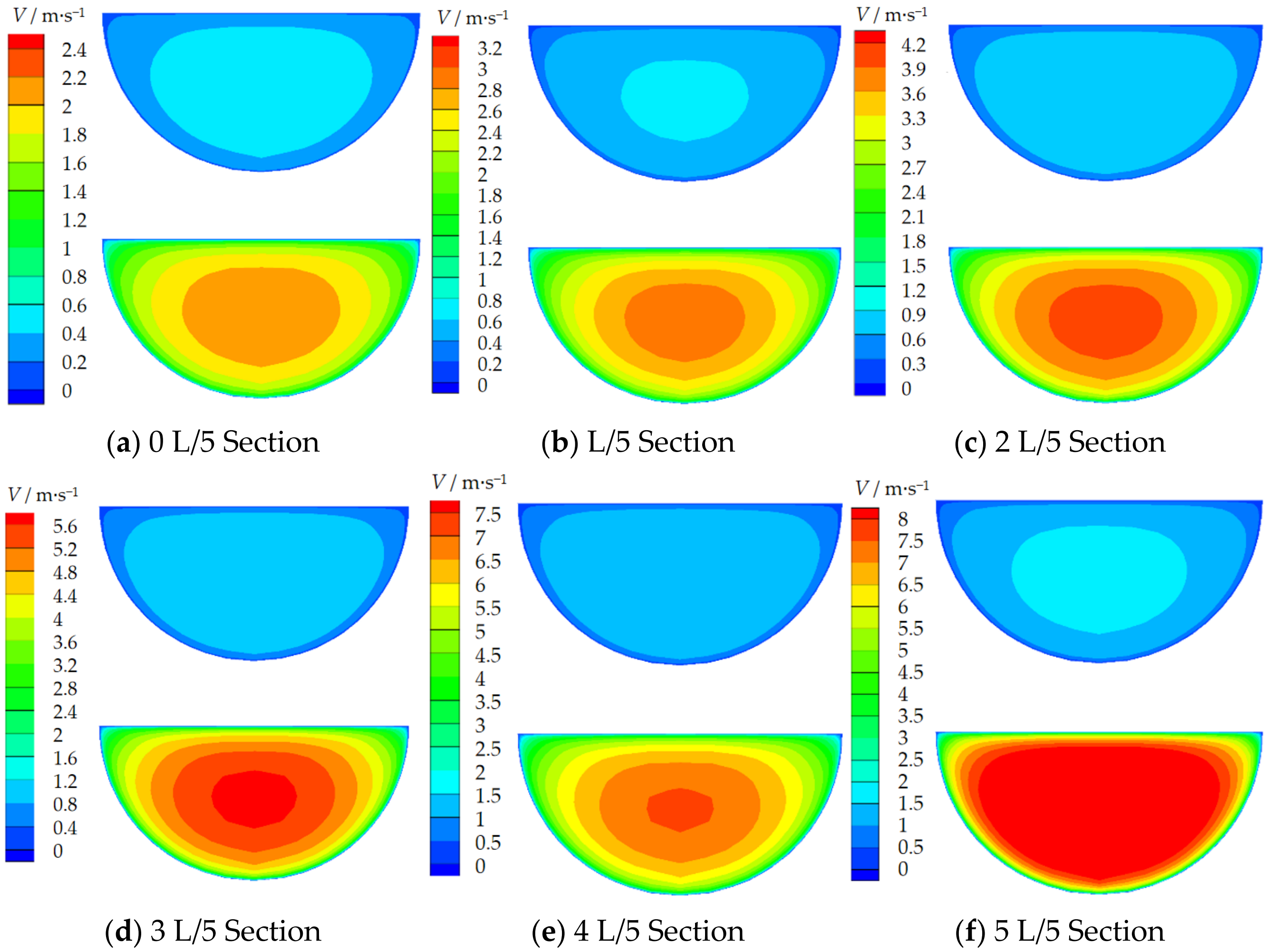

Figure 13. Temperature distributions of the CO_2 and solid material along the PCHE at different cross-sections.

Judging from the heat absorbed by cold CO_2, the thermal performance of the PCHE meets the requirements of the system.

5.2. Flow Characteristics and Thermal Performance of the PCHE under Different Loads

The thermal parameters and boundary conditions vary with the changes in system operating loads. For the purpose of verifying the characteristics of the PCHE under variable running loads, the flow characteristics and thermal performance of the PCHE were numerically simulated when the load varied in the range of ±20% during the discharge time.

The mesh, turbulence model, and methods used in the calculations were consistent with the previous section. However, the boundary conditions were adjusted based on the loads of the energy storage system. The specific inlet and outlet parameters are presented in Table 6. Furthermore, in the following analysis, the direction of the arrows represents the flow direction of CO_2, where "C" denotes the cold side and "H" denotes the hot side.

Table 6. Parameters of the PCHE under different discharge loads.

Unit	Loads/MW	Cold-Side Outlet Pressure/MPa	Hot-Side Outlet Pressure/MPa	Total Mass Flow kg/s	Cold-Side Inlet Temperature/K
	12	27.88	6.5	69.84	298.2
	11	26.4	6.5	66.02	298.2
	10	25	6.5	62.19	298.2
	9	23.55	6.5	58.32	298.2
	8	22.10	6.5	54.43	298.2

Figure 14 presents the distribution of average static pressures along the PCHE under different discharge loads. The pressure on both sides slightly decreases from the inlet to the outlet sides. The magnitude of pressure drop varies with discharge loads. In the cold channel, the pressure of CO_2 increases as the discharge load increases. Additionally, due to the increased flow rate with higher load, the pressure drops of CO_2 experience an increase on both sides.

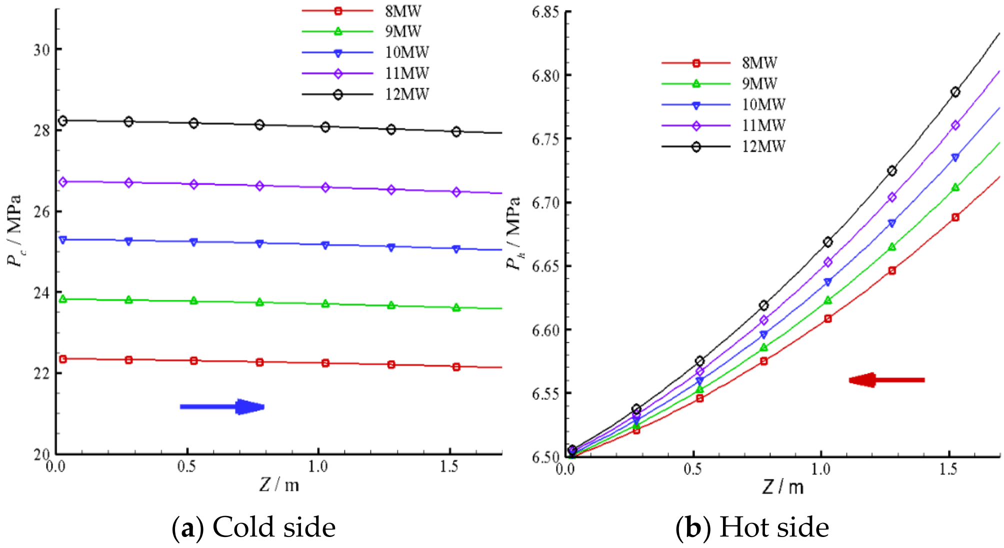

Figure 14. Distribution of average pressures along the PCHE under different discharge loads.

Figure 15 shows the distribution of resistance coefficients along the PCHE both on cold and hot sides under different discharge loads. It can be observed that the resistance coefficients exhibit similar trends under different loads. As the discharge load increases, the resistance coefficients on both sides decrease. It is because the pressure drops increase with the growth of discharge power, mainly due to the increased flow velocity of CO_2 caused by the larger mass flow rate. Since the velocity term appears in the denominator of the resistance coefficient equation, despite the pressure drops increasing with the growth of the discharge load, the resistance coefficient decreases.

Figure 16 displays the flux profiles along the PCHE on both the cold and hot sides under different discharge loads. It can be observed that under the same load, the heat flux of the PCHE gradually rises from the inlet to the outlet on the cold side. The heat flux is consistent at the same position, indicating the accuracy of the calculations. Furthermore, with an increase in the discharge load, the heat flux of the PCHE increases. It is derived from the system flow rate growth as the discharge load increases, resulting in a higher heat capacity recovery requirement for the PCHE.

Figure 17 presents the distribution of average temperatures of CO_2 on both sides under different discharge loads. Figure 18 shows the distribution of average temperatures of the solid material under different discharge loads. From both figures, it observed that along the direction of CO_2 flow on the cold side, the temperatures of CO_2, as well as the solid material of the recuperator, gradually increase on both sides. Furthermore, the growth in temperature increases gradually too. With the increases in discharge load, the mass flow rate increases, and there is a decrease in the inlet temperature of CO_2 on the hot side, while it remains unchanged on the cold side. Therefore, the average temperature along both sides and inside the solid material decreases with the increase in discharge loads. The temperature at the outlet of the cold side slightly decreases from 617.47 K to 611.87 K, which is in the predicted range of the system operation. Then it can be concluded that the performance of the recuperator meets the demand of the system. To make this point concrete, I add the following analysis to the text.

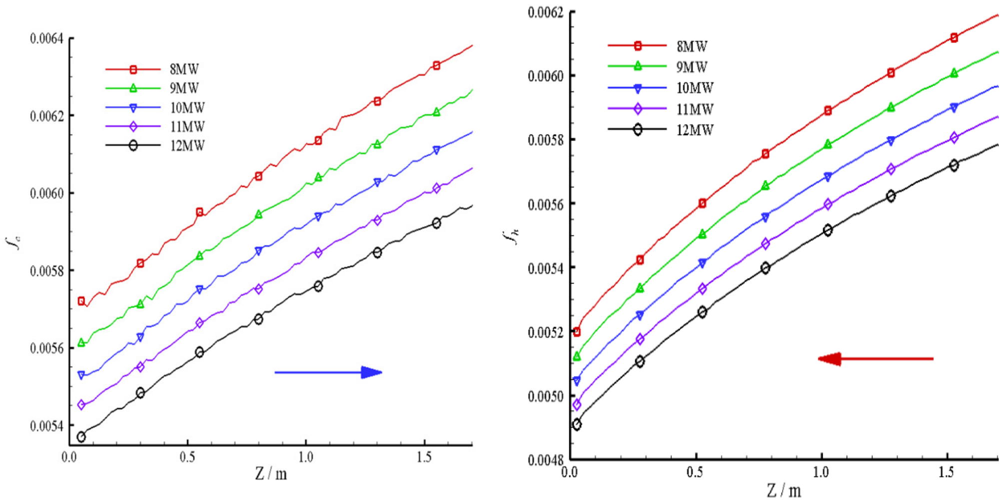

(**a**) Cold side (**b**) Hot side

Figure 15. Distribution of resistance coefficients along the PCHE on both the cold and hot sides under different discharge loads.

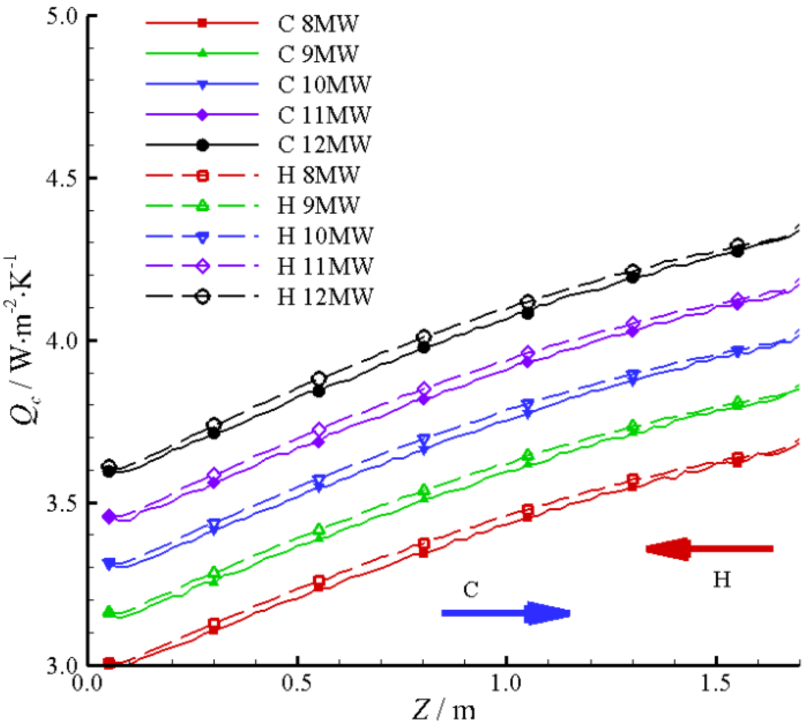

Figure 16. Distribution of heat flux along the PCHE both on the cold and hot sides under different discharge loads.

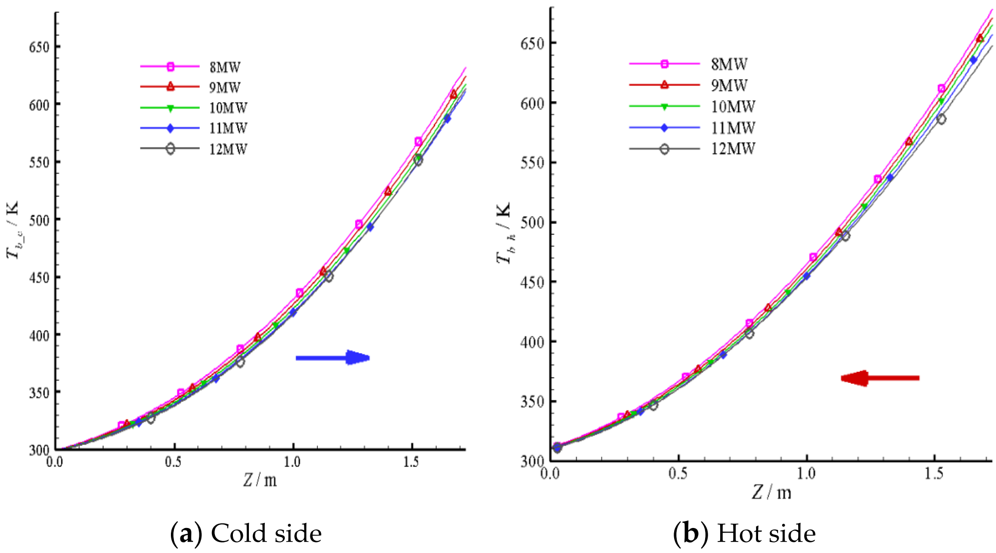

Figure 17. Distribution of average temperatures of CO_2 on both sides under different discharge loads.

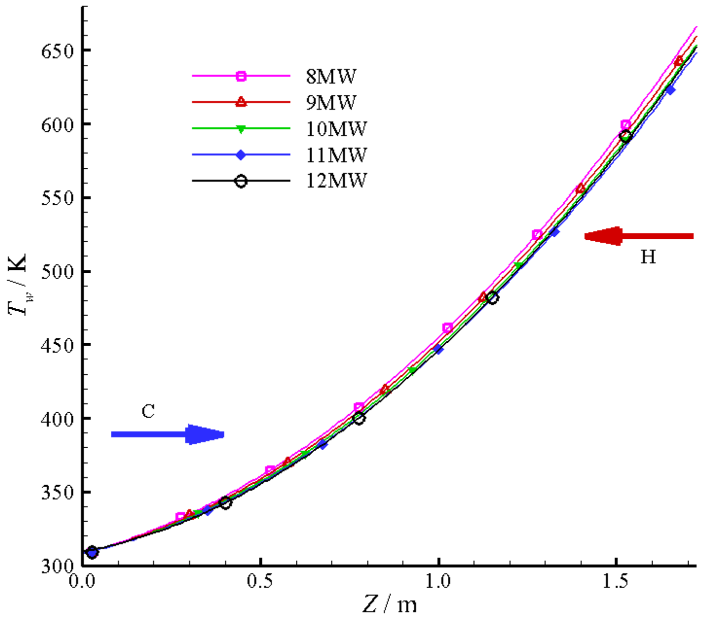

Figure 18. Distribution of the mean temperature of the solid material of the PCHE under different loads.

Figure 19 gives the distribution of *HTC* of CO_2 on both sides under different discharge loads. It is illustrated that along the flow direction of cold-side CO_2, the *HTC* gradually increases on both sides, which is the same as the trend of heat flux along this direction, as shown in Figure 16. It can also be concluded from Figure 19 that as the discharge load increases, the *HTC* in the recuperator increases, which is consistent with the changes in mass flow rate and heat flux. Moreover, with the increasing discharge load, the system mass flow rate of CO_2 increases and the velocity increases, resulting in higher fluid velocity and an increased *HTC*.

Figures 20 and 21 present the distribution of *Nu* and the *HTC* of CO_2 on both sides. It can be observed that along the flow direction of the CO_2 in the cold channel, the *Nu* increases sharply firstly, then gradually increases, and finally decreases, while the *Nu* keeps increasing on the hot side. Moreover, the *Nu* has the same tendency as the *HTC* on the cold side, but it is opposite on the hot side. Since the *HTC* of CO_2 on the cold side first decreases sharply and then increases gradually, although the *HTC* on the cold side increases linearly, the *Nu* first increases sharply, then gradually increases, and finally even decreases. On the other hand, although the *HTC* of CO_2 decreases gradually along the flow direction on the hot side, the thermal conductivity decreases too, resulting in an increasing *Nu*.

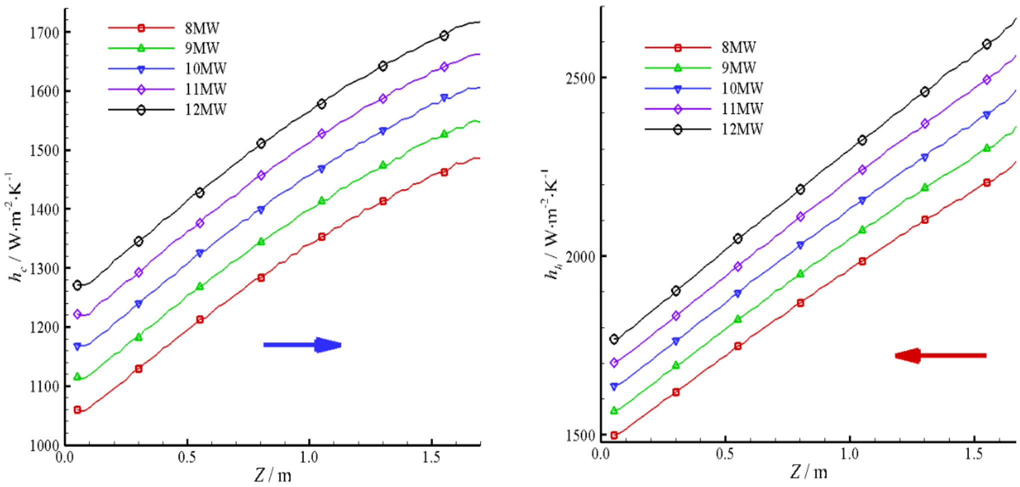

(**a**) Cold side (**b**) Hot side

Figure 19. Distribution of fluid *HTC* on the cold and hot sides of PCHE under different loads.

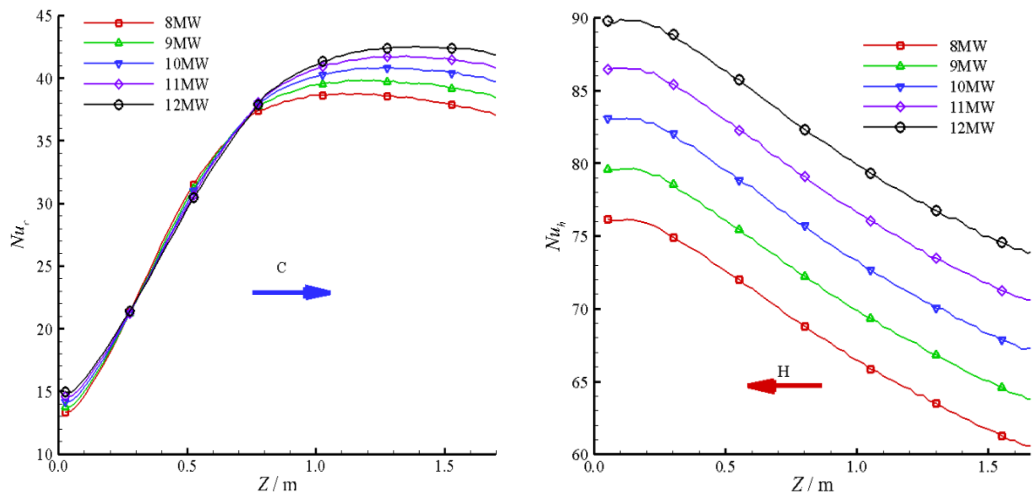

(**a**) Cold side (**b**) Hot side

Figure 20. Distribution of Nusselt numbers of CO_2 on both sides under different loads.

With a growth of discharge loads, the *Nu* on the latter half of the cold side increases gradually, while it grows constantly throughout the hot side. It is also caused by the λ of CO_2 varying differently with the discharge load change. As displayed in Figure 21, the λ of CO_2 exhibits significant variations on the cold side but shows little variation on the hot side. That is mostly because the pressure of CO_2 on the cold side changes greater than that on the hot side.

From the above analysis, the conclusions can be drawn that the PCHE can meet the requirement of the LCES operating within a range of $\pm 20\%$.

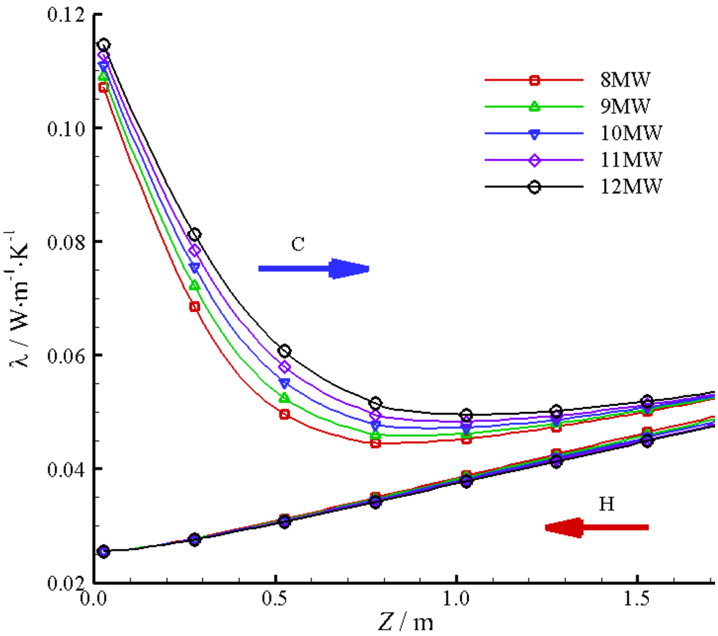

Figure 21. Distribution of thermal conductivity of CO_2 both on the cold and hot sides under different loads.

6. Conclusions

In this study, the thermal design of a printed circuit recuperator used in the LCES was completed. The numerical solution method adopted was verified, and the flow characteristics and thermal performance of the recuperator under design parameters were analyzed. The effect of different discharge loads on the flow characteristics and thermal performance of the fluid was investigated. The key findings are as follows:

1. The thermal design of the PCHE was completed. The structural form and dimensions of the PCHE have been determined.
2. The flow characteristics and heat transfer capability analysis of the PCHE adopting different turbulence models were compared. The SST k-ω model matched the experimental data best.
3. Under design conditions, the resistance coefficient of the CO_2 on the cold side increased gradually, from the inlet to the outlet of the PCHE, while decreasing gradually on the hot side. The variations in the flow velocity of CO_2 on both sides were consistent with the changes in the resistance coefficient. The average temperature of CO_2 on the cold side increased rapidly, while the decline rate of temperature on the hot side gradually slowed down. Furthermore, the *Nu* of CO_2 on the cold side has a sharp increase firstly followed by a slow increase, and finally exhibits a gradual decrease. Conversely, the *Nu* exhibits a gradual increase on the hot side.
4. The flow characteristics and heat transfer of CO_2 in the PCHE under different discharge loads were studied. As the discharge load of LCES increased, the pressure drop of CO_2 in both the cold and hot sides increased, while the resistance coefficient on both sides decreased gradually. The *HTC* of CO_2 on both sides gradually increased. The *Nu* of the CO_2 on the front half of the cold side increased sharply while changing a little on the rear half. The *Nu* of CO_2 increased gradually along the flow on the hot side. From the perspective of the temperature and heat transfer capacity of the CO_2 on both sides under different loads, the designed PCHE meets the requirements for variable operating conditions of the energy storage system.

Author Contributions: Methodology, M.X.; Software, Y.S. and M.X.; Formal analysis, M.X.; Data curation, M.W.; Writing—original draft, Z.L.; Writing—review & editing, M.W.; Supervision, M.X.; Funding acquisition, Z.L. All authors have read and agreed to the published version of the manuscript.

Funding: The authors are grateful for this work being supported by the National Natural Science Foundation of China (Grant No. 52076168).

Institutional Review Board Statement: Not applicable.

Informed Consent Statement: Not applicable.

Data Availability Statement: The data presented in this study are available on request from the corresponding author. The data are not publicly available due to privacy.

Conflicts of Interest: The authors declare no conflict of interest.

Nomenclature

Abbreviations	
ACAES	Adiabatic compressed air energy storage system
CAES	Compressed air energy storage system
EVR	Energy storage (kWh·m^{-3})
CCES	Compressed carbon dioxide energy storage system
CCHP	Systems combined with cooling heating and power systems
HTC	Heat transfer coefficient
LMTD	Logarithmic mean temperature difference
PCHE	Printed circuit heat exchanger
RTE	System round-trip efficiency
TEES	Thermo-electrical energy storage system
Symbol	
A	Heat transfer area (m^2)
D_h	Hydraulic diameter of the fluid channel
f_d	Darcy resistance coefficient
G	Mass flow rate per unit area (kg·s^{-1}·m^{-2})
h	Convective heat transfer coefficient (W·m^{-2}·K^{-1})
Nu	Nusselt number
Pr	Prandtl number
Q	Heat transfer capacity (W)
Re	Reynolds number
U	Heat transfer coefficient (W·m^{-2}·K^{-1})
δ	Thickness of the heat exchanger wall (m)
λ	Thermal conductivity of the wall material (W·m^{-1}·K^{-1})
R_w	Fouling thermal resistance

References

1. Budt, M.; Wolf, D.; Span, R.; Yan, J. A Review on Compressed Air Energy Storage: Basic Principles, Past Milestones and Recent Developments. *Appl. Energy* **2016**, *170*, 250–268. [CrossRef]
2. Borri, E.; Tafone, A.; Zsembinszki, G.; Comodi, G.; Romagnoli, A.; Cabeza, L.F. Recent Trends on Liquid Air Energy Storage: A Bibliometric Analysis. *Appl. Sci.* **2020**, *10*, 2773. [CrossRef]
3. Chae, Y.J.; Lee, J.I. Thermodynamic Analysis of Compressed and Liquid Carbon Dioxide Energy Storage System Integrated with Steam Cycle for Flexible Operation of Thermal Power Plant. *Energy Convers. Manag.* **2022**, *256*, 115374. [CrossRef]
4. Wang, M.; Zhao, P.; Wu, Y.; Dai, Y. Performance Analysis of a Novel Energy Storage System Based on Liquid Carbon Dioxide. *Appl. Therm. Eng.* **2015**, *91*, 812–823. [CrossRef]
5. Zhang, Y.; Yang, K.; Hong, H.; Zhong, X.; Xu, J. Thermodynamic Analysis of a Novel Energy Storage System with Carbon Dioxide as Working Fluid. *Renew. Energy* **2016**, *99*, 682–697. [CrossRef]
6. Liu, S.; Wu, S.; Hu, Y.; Li, H. Comparative Analysis of Air and CO_2 as Working Fluids for Compressed and Liquefied Gas Energy Storage Technologies. *Energy Convers. Manag.* **2019**, *181*, 608–620. [CrossRef]
7. Alami, A.H.; Hawili, A.A.; Hassan, R.; Al-Hemyari, M.; Aokal, K. Experimental Study of Carbon Dioxide as Working Fluid in a Closed-Loop Compressed Gas Energy Storage System. *Renew. Energy* **2019**, *134*, 603–611. [CrossRef]
8. Zhang, Y.; Lin, Y.; Lin, F.; Yang, K. Thermodynamic Analysis of a Novel Combined Cooling, Heating, and Power System Consisting of Wind Energy and Transcritical Compressed CO_2 Energy Storage. *Energy Convers. Manag.* **2022**, *260*, 115609. [CrossRef]
9. Haynes, B.S. High-Effectiveness Micro-Exchanger Performance. In Proceedings of the AIChE Spring, New Orleans, LA, USA, 10–14 March 2002.

10. Dostál, V.; Driscoll, M.; Hejzlar, P. *A Super Critical Carbon Dioxide Cycle for Next Generation Nuclear Reactors*; Massachusetts Institute of Technology: Cambridge, MA, USA, 2011.
11. Meshram, A.; Jaiswal, A.K.; Khivsara, S.D.; Ortega, J.D.; Ho, C.; Bapat, R.; Dutta, P. Modeling and Analysis of a Printed Circuit Heat Exchanger for Supercritical CO_2 Power Cycle Applications. *Appl. Therm. Eng.* **2016**, *109*, 861–870. [CrossRef]
12. Wen, Z.-X.; Lv, Y.-G.; Li, Q.; Zhou, P. Numerical Study on Heat Transfer Behavior of Wavy Channel Supercritical CO_2 Printed Circuit Heat Exchangers with Different Amplitude and Wavelength Parameters. *Int. J. Heat Mass Transf.* **2020**, *147*, 118922. [CrossRef]
13. Zhang, K.; Wei, W.; Sun, Y.; Wu, Q.; Tang, M.; Lu, M. Design and Optimization of the Inlet Header Structure in Microchannel Heat Exchanger Based on Flow Distribution Uniformity. *Appl. Sci.* **2022**, *12*, 6604. [CrossRef]
14. Simanjuntak, A.; Lee, J.Y. Mechanical Integrity Analysis of a Printed Circuit Heat Exchanger with Channel Misalignment. *Appl. Sci.* **2020**, *10*, 2169. [CrossRef]
15. Xin, F.; Ma, T.; Wang, Q. Spray Etching Rate Development of Stainless Steel in the Etchant for Printed Circuit Heat Exchanger Channels. *Energy Procedia* **2017**, *105*, 4828–4835. [CrossRef]
16. Chu, W.; Li, X.; Ma, T.; Chen, Y.; Wang, Q. Experimental Investigation on SCO_2-Water Heat Transfer Characteristics in a Printed Circuit Heat Exchanger with Straight Channels. *Int. J. Heat Mass Transf.* **2017**, *113*, 184–194. [CrossRef]
17. Cheng, K.; Zhou, J.; Zhang, H.; Huai, X.; Guo, J. Experimental Investigation of Thermal-Hydraulic Characteristics of a Printed Circuit Heat Exchanger Used as a Pre-Cooler for the Supercritical CO_2 Brayton Cycle. *Appl. Therm. Eng.* **2020**, *171*, 115116. [CrossRef]
18. Kwon, D.; Kim, S.; Jung, W.; Jeong, S. Experimental Investigation of Heat Transfer Coefficient of Mini-Channel PCHE (Printed Circuit Heat Exchanger). *Cryogenics* **2018**, *92*, 41–49. [CrossRef]
19. Xu, M.; Zhao, P.; Huo, Y.; Han, J.; Wang, J.; Dai, Y. Thermodynamic analysis of a novel liquid carbon dioxide energy storage system and comparison to a liquid air energy storage system. *J. Clean. Prod.* **2020**, *242*, 118437. [CrossRef]
20. Gnielinski, V. New Equations for Heat and Mass Transfer in Turbulent Pipe and Channel Flow. *NASA STI/Recon Tech. Rep. A* **1976**, *41*, 8–16.
21. Kader, B.A. Temperature and Concentration Profiles in Fully Turbulent Boundary Layers. *Int. J. Heat Mass Transf.* **1981**, *24*, 1541–1544. [CrossRef]
22. Nikitin, K.; Kato, Y.; Ngo, L. Printed Circuit Heat Exchanger Thermal–Hydraulic Performance in Supercritical CO_2 Experimental Loop. *Int. J. Refrig.* **2006**, *29*, 807–814. [CrossRef]
23. Ngo, T.L.; Kato, Y.; Nikitin, K.; Ishizuka, T. Heat Transfer and Pressure Drop Correlations of Microchannel Heat Exchangers with S-Shaped and Zigzag Fins for Carbon Dioxide Cycles. *Exp. Therm. Fluid Sci.* **2007**, *32*, 560–570. [CrossRef]
24. Kim, D.E.; Kim, M.H.; Cha, J.E.; Kim, S.O. Numerical Investigation on Thermal–Hydraulic Performance of New Printed Circuit Heat Exchanger Model. *Nucl. Eng. Des.* **2008**, *238*, 3269–3276. [CrossRef]
25. Kim, S.G.; Lee, Y.; Ahn, Y.; Lee, J.I. CFD Aided Approach to Design Printed Circuit Heat Exchangers for Supercritical CO_2 Brayton Cycle Application. *Ann. Nucl. Energy* **2016**, *92*, 175–185. [CrossRef]
26. Kim, I.H.; Sun, X. CFD Study and PCHE Design for Secondary Heat Exchangers with FLiNaK-Helium for SmAHTR. *Nucl. Eng. Des.* **2014**, *270*, 325–333. [CrossRef]
27. Ishizuka, T.; Kato, Y.; Muto, Y.; Nikitin, K. Thermal-hydraulic characteristics of a printed circuit heat exchanger in a supercritical CO_2 loop. *Bull. Res. Lab. Nucl. React.* **2006**, *30*, 109–116.
28. Hesselgreaves, J.E.; Law, R.; Reay, D.A. *Compact Heat Exchangers: Selection, Design and Operation: Second Edition*; Butterworth-Heinemann: Oxford, UK, 2016; p. 484.